Channel-based Antenna Synthesis for Improved In-vehicle UWB MB-OFDM Communications

Ashwani Sharma[1,2] *Ignacio J. Garcia Zuazola*[3] *Ramón Martínez*[4] *Asier Perallos*[2] *John C. Batchelor*[5]

[1] *Eletrical Engineering Department, Indian Institute of Technology Ropar, Rupnagar, Punjab 140001, India*
[2] *Deusto Institute of Technology - DeustoTech, University of Deusto, 48007, Bilbao, Spain*
[3] *Faculty of Technology, University of Portsmouth, Portsmouth, Hampshire, PO1 3DJ, UK*
[4] *SSR Department, ETSI Telecommunication, Universidad Politécnica de Madrid, Ciudad Universitaria, 28040, Madrid, Spain*
[5] *Department of Engineering and Digital Arts, University of Kent, Canterbury, Kent, CT2 7NT, UK*
** E-mail: ashwani.sharma@iitrpr.ac.in, perallos@deusto.es, igarcia@theiet.org, ramon@gr.ssr.upm.es, j.c.batchelor@kent.ac.uk*

Abstract: Ultra-Wide Band (UWB) is an attractive technology for innovative in-vehicle wireless communications requiring high data rates and MultiBand Orthogonal Frequency Division Multiplexing (MB-OFDM) a suitable scheme for the accomplishment due to its high performance, low-power and low-cost characteristics. To contribute towards improved UWB MB-OFDM communications inside vehicles, a channel-based antenna synthesis technique to customize in-vehicle UWB antennas that reduce “blind spots" in the communication channel is proposed and presented. For the realization, a comprehensive analysis was utilized and comprised an in-car channel evaluation; including BER estimations, and radiation pattern-and-source syntheses. The channel was measured using a standard antenna to set-up the base of the experiments and the distribution of the impulse responses (IRs) and signal-to-noise ratios (SNRs) in the vehicle’s passenger plane shown. The currently available IEEE 802.15.3a channel models were perceived unrealistic for the in-vehicle application and the reason of measuring the channel practically. Using these specific channel measurements, the synthesized pattern is unveiled and consequently the channel-based antenna synthesis technique used to predict the antenna source. The antenna with optimized pattern-and-source showed an improved BER performance compared to the standard antenna in this application; that is a figure of merit of 37.73% minimized “blind spots".

1 Introduction

Ultra-Wide Band (UWB) wireless communciation in-vehicles is very attractive for the cost-reduction of traditional wiring and for the provision of mobility to passengers eager for multimedia applications with high data rates inside vehicles [1, 2]. The unlicensed UWB spectrum is a low-cost solution and its low range of operation adequate for the vehicle dimensions. In 2002, the US Federal Communications Commission (FCC) allocated the frequency band, 3.1 - 10.6 GHz, for unlicensed operation of UWB radios [3] and a maximum allowed Power Spectral Density (PSD) of -41.3 dBm/MHz. The low power allows ranges < 10 m and its wide BandWidth (BW) a high data rate of $\sim$480 Mbps. Therefore, UWB emerged as a promising technology for short-range high data rate wireless communications [4]. For instance, in in-vehicle applications, the UWB is potentially attractive for the delivery of high data rates with spatial capacity and multipath immunity in a low power operation and low cost solution [1, 2].

The MultiBand Orthogonal Frequency Division Multiplexing (MB-OFDM) is a robust competitor for the standardization of UWB [5, 6], and the IEEE 802.15 standardization group organized a task 3a [7] for proposing a physical layer based on UWB signaling [8, 9]. The European Computer Manufacturers Association (ECMA) standard, has adopted UWB MB-OFDM recently [10]. UWB MB-OFDM was adopted in [1, 2] for in-vehicle communications due to its slightly more immunity to Gaussian noise [11] and lower complexity [12, 13] compared to its competitor Direct Sequence UWB (DS-UWB). In [14], design parameters of a MB-OFDM system for a specific channel were presented using a physical (PHY) architecture and evaluated assuming UWB Channel Models (CMs) developed under the IEEE 802.15.3a working group, CM1, CM2, CM3, and CM4, for several line of sight (LOS) and non-line of sight (NLOS) scenarios [14, 15] which accounted for the clustering effects of the channel [16].

Multipath propagation characteristics inside vehicles (of waves impacting predominantly the vehicle fuselage, windows and seats) are highly complex to model (i.e., the distribution of the received signal envelope) and new measurements (experimental data) is designated for different scenarios.

In the literature, various contributions [17–24] were dedicated to study in-vehicle channels experimentally, however, scarce datapoints of the scenario determined the CMs based on static locations of replaced wires within the car. In these studies, single element omni-directional antennas were used and perceived inexpensive compared to more sophisticated Adaptive Antenna Systems (AAS) (i.e, smart antennas). The access point (AP) antenna was favored in the middle of the car ceiling [25] for high bit rates due to a good power distribution to mobile equipment (ME) and the in-vehicle channel was studied experimentally for this AP location in [1, 2].

In the present study, the authors examine an alternative to omni-directional antenna as AP and a fully-quantified channel, which uses received data responses in the passenger plane (PP) and delimited in Fig. 1, is measured for the realization. As a consequence a synthesized antenna radiation pattern is optimized which minimizes the “blind spots", later defined, in the passenger plane and improve the Bit-Error-Rate (BER) of the system considerably as a result. Though, channel coding schemes can improve BER performance in channels with white noise level, they are of little benefit in deeply faded channels, where the signal is dominant by the noise, hence, erroneous codes are received. In this study, we focus to improve the received signal power by determining the antenna radiation pattern, hence, the multipath distribution arriving at deeply faded locations is improved. The channel was initially characterized by measurements using a standard antenna and aimed to provide a realistic modeling to custom prototypes. Existing antennas in literature, from planar to three dimension (3-D) prototypes (patch/slots and printed monopoles) have dissimilar performance [26–31], and that supports customizing antennas for specific applications.

Efforts have been made to customize antennas for different applications and that must account for the size, BW, transition, integration and the associated efficiency. For instance, in [32], UWB antennas for wireless communications and detection (using the 3.5 to 9.9 GHz band) have been presented. However, because of the wideband characteristic, they suffer from inherent interference of neighboring transmissions (i.e., WLAN); for the alleviation, band-notched antennas have been reported in [28, 32]. Band Pass Filter (BPF) like response antennas are also attractive to reduce complexity in transceivers and a BPF-like UWB antenna has been presented in [33]. Although the vast number of antennas in the literature, in this manuscript, a pattern-and-source of a prospective antenna is optimized for the in-vehicle application. It will be shown that the aforementioned UWB antenna response leads to an improved BER performance in the passenger plane as a result of lowering the "blind spots" in this plane by providing a uniform synthesized pattern. Although a traditional way to reduce the blind spots inside the vehicle would be to use Multiple Input Multiple Output (MIMO) antenna configurations, however, a single antenna configuration is preferred as a low cost approach because the capacity improvement brought by MIMO is made upon an increase in the costs associated with hardware, the multiple antenna prototypes and accompanying front-ends[34]. Furthermore, to configure MIMO antennas inside vehicle, in-car channel measurements must also be performed. In the case where users/manufacturers are ready to pay extra for MIMO to add more functionality such as capacity, the proposed channel-based antenna synthesis is equally valid for MIMO.

The standard antenna used for the channel measurements will be shown to report non-uniform signal-to-noise ratios (SNRs) in the passenger plane and the need to optimize the antenna radiation pattern for the in-vehicle scenario. This drawback contributes to blind spots (defined for BERs $> 10^{-5}$ as a target BER threshold for UWB MB-OFDM, [14]) which can be minimized using antenna radiation patterns with gains effectively distributed in the passenger plane, thus, improving the received SNR levels of the system. To make this feasible, the channel-based antenna synthesis is used to optimize the antenna pattern and takes into account a pre-measured in-car channel using the standard antenna; including BERs in a realistic scenario, and a radiation pattern-and-source synthesis of a prospective antenna candidate.

The rest of the paper is organized as follows. Section 2 introduces the in-vehicle channel, defines the passenger plane, and the inefficient UWB communications in-car using the standard antenna (the optimization problem). Section 3 presents the channel-based antenna synthesis which comprises a fully-integrated mathematical analysis for an in-depth study of the in-car channel whose behavior deficiencies are used for the optimization; including the in-vehicle channel measurements, Matlab/Simulink BER-SNR simulations, antenna space-factor (SF) calculation and the radiation pattern-and-source synthesis. The implementation of the channel-based antenna synthesis is given in Section 4 with the following subsections: Section 4.1 presents the experimentally measured in-vehicle channel using the standard antenna, including the received Impulse Responses (IRs) and SNRs. Section 4.2, the regular simulations of the UWB MB-OFDM system using MATLAB/Simulink with compared BER performance for various analytical channels, Additive White Gaussian Noise (AWGN), CM1-4, and that measured experimentally; this is performed to establish the essential BERs and desired radiation pattern of the antenna for the improved in-vehicle communications. Section 4.3, the optimized radiation pattern-and-source of the prospective antenna with corresponding current and phase. Section 5 presents the comparative results of the BER distribution and blind spot experience using the standard and the prospective antennas. The paper is concluded in Section 6.

2 The In-vehicle channel

The in-vehicle system configuration showing the vehicle geometry and the access point (AP) and mobile equipment (ME) locations is depicted in Fig. 1. The access point and the mobile equipment antennas connected to their respective UWB MB-OFDM transmit/receive equipment (transceivers) and measurements were taken at the passenger plane (PP) which is set 0.8 m below the ceiling, *"This is the most likely location for the mobile/fixed equipment while minimizing field exposure to occupants"* [1, 2]. The passenger plane is therefore defined at $z = 0.6$ m, with mobile equipment locations judiciously distributed over the $(x, y, 0.6)m, \forall x \in (0, 2)m; y \in (0, 1.2)m$.

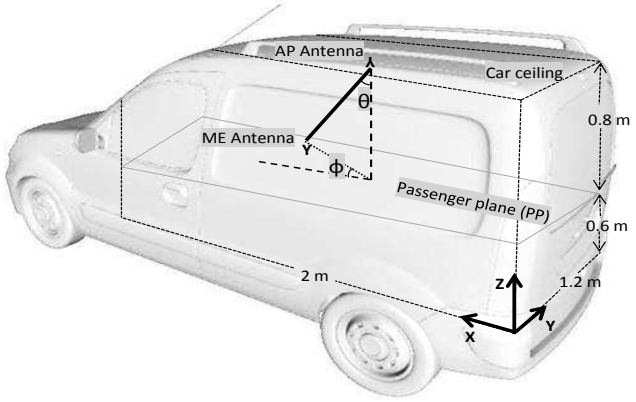

Fig. 1: The in-vehicle system configuration.

The in-car scenario was assumed static, using a closed-window environment without occupants and a motionless vehicle. As in [1] the authors will corroborate that the occupants do not cause significant effect on the results due to the broadband nature of the UWB. The positions of the mobile equipment with respect to the access point essentially determine every communication link within the channel (the IRs and received SNRs later presented in Section 4.1). Because of the differ locations of mobile equipment that are present in the passenger plane, the channel power delay profiles (PDP) vary as it does the BER.

To account for these variations, the BER response is optimized for every point $(x, y, 0.6)m$ of the passenger plane grid (later defined in Section 4). The $BER(x, y)$ distribution depends on the radiation pattern of the antenna since at different angles of the main lobe, the power strength varies. It will be shown in Section 5 that a commercial antenna (the standard) from Wisair Ltd., characterized by an omni-directional pattern, leads to poor BER responses for this in-vehicle application. Since we aim to provide $BER(x, y)$ lower than a target BER $\eta = 10^{-5}$ (a desired threshold in realistic UWB channels [14]), the undesired BERs are determined as blind spots. The blind-area response is used for comparison purposes between the standard and the prospective antennas and defined as,

$$\%\text{Blind-Area} = \frac{\text{PP grid with } BERs > \eta}{\text{Total dimension of the PP in m}^2} 100 \qquad (1)$$

2.1 The optimization problem

Ideally, the blind spots should be kept to minimum and the antenna customized for this purpose. Antennas are generally universal and their tunning for defined scenarios (such as in-vehicle) attractive. For the customization, the channel-based antenna synthesis targets for foremost BERs in the passenger plane with an optimization criteria given by,

$$\begin{cases} \text{Pattern-and-source synthesis of an antenna} \\ \text{such that} \\ \%\text{Blind-Area (1) is minimum} \end{cases} \qquad (2)$$

For the realization of (2), the in-car channel was analyzed and measurements using the standard antenna collected. The desired BERs

distributed over the passenger plane were found and a antenna radiation pattern of gains better disseminated in-car tailored using the channel-based antenna synthesis, next.

3 The channel-based antenna synthesis

In this section, the channel-based synthesis for the prospective antenna having a tailored radiation pattern for the in-car application is detailed. In essence, the synthesis method complies with (2) and uses a concise process of three main stages. A flow chart showing the complete process is shown in Fig. 2 and the break-through of stages 1-3 subsequently detailed.

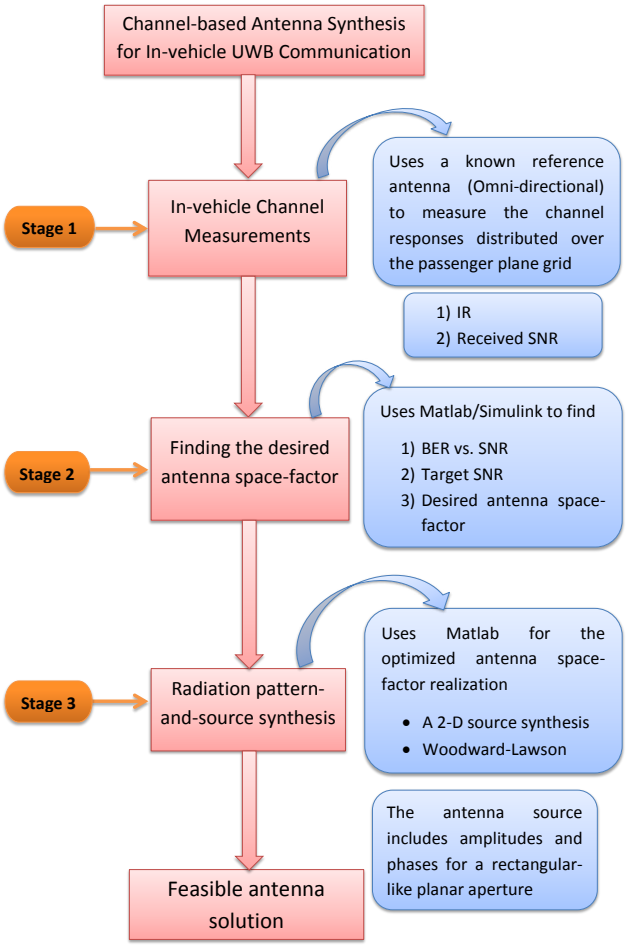

Fig. 2: Flow-chart showing the stages of the proposed channel-based antenna synthesis.

3.1 *Stage-1 : In-vehicle channel (measuring arrangements)*

Multipath intensifies with the car body which acts as a reverberation chamber. The BER depends on the received SNR (SNR_{Rcv}) and IR, $h(t)$ [35] of the channel, and the receiver processing. The SNR_{Rcv} takes into account the path-loss and thus includes the actual channel gain. Since the channel response varies depending on the mobile equipment whereabouts, the SNR_{Rcv} and $h(t)$ are location dependent and the BER in such a circumstance is given by [35]

$$BER(x, y) = f[SNR_{Rcv}(x, y), h(t, x, y)], \qquad (3)$$

where $f[\cdot]$ is the complex relation which transforms the characteristics of the channel (SNR and IR) into the evaluated BER performance and includes the processing at the MB-OFDM receiver.

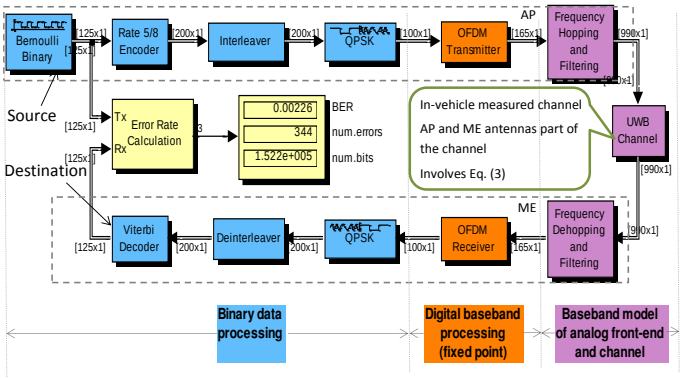

Fig. 3: The adapted UWB MB-OFDM model from MATLAB Simulink [36].

Both, the $SNR_{Rcv}(x, y)$ and $h(t, x, y)$ were experimentally measured at this stage and are presented in Section 4.1. The resulting channel profiles using the known reference omni-directional antenna (the standard) are hereby defined as $SNR^0_{Rcv}(x, y)$ and $h^0(t, x, y)$. The estimated $BER(x, y)$ is presented in Stage-2, subsequently.

3.2 *Stage-2 : Finding the desired antenna space-factor*

For the desired antenna space-factor, the $BER(x, y)$ is first found for every point in the passenger plane grid and using the previously measured (Stage-1) $SNR^0_{Rcv}(x, y)$ and $h^0(t, x, y)$; the result is denoted as $BER^0(x, y)$. The channel model was adopted from Matlab Simulink - UWB MB-OFDM BER simulator [36], and measured impulse responses (describe realistically the in-car scenario) were considered in this statistical channel. This simulator is presented in Fig. 3 where the essential elements in block diagram are shown and well differentiates the access point (AP) transmit and mobile equipment (ME) receive paths.

In essence, Matlab/Simulink is used to resolve for the closed-form solution of (3) while providing a realistic UWB channel and BER performance. The model is now described with emphasis to the adapted UWB channel block.

Basically, 10^7 bits were sent from source (a Bernoulli Binary data generator) to destination (a Viterbi Decoder) across the UWB channel. The encoder, interleaver, modulator and OFDM transmitter blocks are at the transmitter and the latest incorporates the channel estimation present in majority of current communication systems using 122 subcarriers, 22 pilots, 128-point FFTs. The model presents multipath resistance from cyclic prefix of 60 ns [36]. Though the instantaneous channel estimation error affects the final performance, the proposed synthesis method rely on average BER simulations. This is because the antenna can not be synthesized in the instantaneous manner but the average. Both, the transmitted (Tx) and received (Rx) bits are compared by the Error rate Calculator for the BERs. The UWB channel block was adapted beforehand to contemplate for the channel measurements of the in-car scenario (Stage-1), where the access point and mobile equipment antennas were considered as part of the channel and results normalized; meaning that changing the type of antenna either at the mobile equipment or the access point or both should not change the channel-based antenna synthesis results.

Therefore, the custom channel block uses user-defined parameters to comprise the measured channel responses ($SNR^0_{Rcv}(x, y)$ and $h^0(t, x, y)$); this makes use of tangible data from realistic antenna radiation patterns, multipath components and channel impairments. The simulated results are presented in Section 4.2. To overcome the unacceptably high BER performance (compared to the η) given by the standard antenna, the $SNR_{Rcv}(x, y)$ are improved (focused signals) by a tailored antenna radiation pattern. This is detailed in Stage-3, Section 3.3 and is performed using pattern synthesis [37] which is described subsequently.

For the tailored antenna radiation pattern, the BER-SNR is first estimated using the adapted Matlab/Simulink model for corresponding $h^0(t,x,y)$ in the passenger plane grid. This finds the required SNR (target SNR=γ) to corresponding target BER η and is performed iteratively using the following entries:

$$\begin{aligned} &\text{For } \forall x \in (0,2); y \in (0,1.2) \\ &\quad \begin{cases} \text{find} \quad SNR > 0 \quad \text{such that} \\ f[SNR, h^0(t,x,y)] = \eta \end{cases} \\ &\quad \gamma(x,y) \quad \Leftarrow SNR \end{aligned} \tag{4}$$

Using the resulting $\gamma(x,y)$ from (4) and the measured SNR^0_{Rcv} (Stage-1, Section 3.1), the tailored radiation pattern is estimated by means of a synthesized antenna source. This source synthesis is presented in Stage-3, Section 3.3, and relies on the space-factor of the antenna for the estimation. This is outlined next.

The radiation pattern of an antenna (continuous source) in free-space is given [37] by:

$$\text{Total pattern} = EF \times SF \tag{5}$$

where the Element Factor (EF) is the radiation characteristics of a single source and SF is the radiation pattern as a result of all the contributions and interactions from the continuous sources that form the antenna physical aperture of Fig. 4.

Because the standard antenna is actually a single element antenna, a single point source applies and hence $SF = 1$ and $EF = EF^0$ (the EF of the omni-directional pattern of the standard antenna). In this case, (5) becomes,

$$\text{Total pattern (standard antenna)} = EF^0 \approx \sqrt{SNR^0_{Rcv}(x,y)} \tag{6}$$

where $\sqrt{SNR^0_{Rcv}(x,y)}$ corresponds to the signal amplitudes received in the passenger plane grid, and previously measured in Stage 1, Section 3.1 using the standard antenna; this approximation is valid for frequency selective channels. The relation in (6) is intended since the antenna pattern corresponds to the received signal amplitude which is proportional to square root of received signal power and hence of received SNR.

For the tailored radiation pattern, the space-factor of the new antenna is optimized and denoted hereby as the desired space-factor ($SF_d(x,y)$). The computation of $SF_d(x,y)$ is performed using Matlab and uses the experimentally measured SNR^0_{Rcv} to account for the realistic effects of the in-car scenario.

In essence, the modeling of the new pattern uses the $\gamma(x,y)$ and the $SF_d(x,y)$, so that (5) rearranges as,

$$\sqrt{\gamma(x,y)} = EF^0 \times SF_d(x,y), \tag{7}$$

where $x \in (0,2)$; $y \in (0,1.2)$. Substituting EF^0 using (6), and solving (7) for the $SF_d(x,y)$ we obtain,

$$SF_d(x,y) = \sqrt{\frac{\gamma(x,y)}{SNR^0_{Rcv}(x,y)}}. \tag{8}$$

In (8), we have the ratio of two SNRs, therefore, the noise on average is not anticipated to affect the space-factor calculations logically. (8) is a requisite in Stage-3, Section 3.3, next.

3.3 *Stage-3 : Radiation pattern-and-source synthesis*

The theoretical analysis behind the radiation pattern-and-source synthesis of the prospective antenna is accomplished and detailed subsequently. The general form of $SF_d(x,y)$ from (8), is adapted to contemplate the single antenna source and in-car channel. For this purpose, we assumed a 2-D rectangular-like patch antenna as

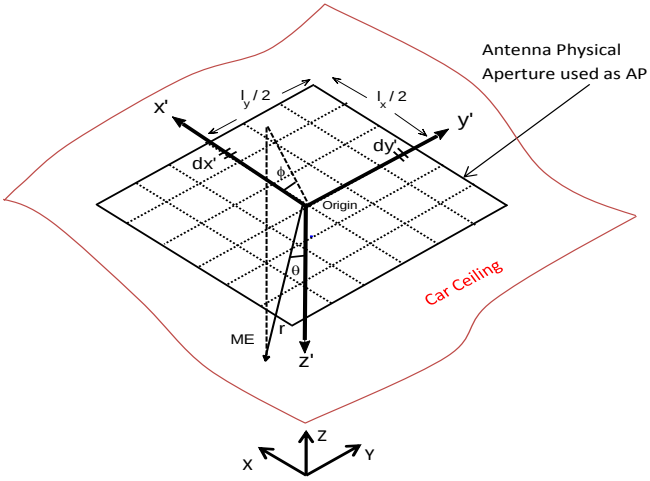

Fig. 4: The geometry of the antenna physical aperture used as access point (AP).

the source with a physical aperture of dimensions $l_x \times l_y$ and local coordinate system (x', y', z'); this is presented in Fig. 4.

The $SF_d(x,y)$ takes the form of $SF_d(\theta,\phi)$ to account for the spherical coordinate system of the antenna whose aperture (effective area) is predominantly related to the passenger plane dimensions, Fig. 1. θ and ϕ are given by the following transformation equations and calculated geometrically as,

$$\begin{aligned} \theta &= \tan^{-1}\left[\frac{\sqrt{(x-1.0)^2 + (y-0.6)^2}}{0.8}\right], \\ \phi &= \tan^{-1}\left[\frac{(0.6-y)}{(1.0-x)}\right]. \end{aligned} \tag{9}$$

The origin of the antenna aperture (Fig. 4) is the center of the access point (AP) (Fig. 1) with coordinates x=1 m, y=0.6 m and z=1.4 m. Hence, $x = x' + 1; y = y' + 0.6; z = 1.4 - z'$.

The general form of $SF(\theta,\phi)$ for a continuous source (a single source also applies) is given by [37], Chap. 7, as,

$$\begin{aligned} SF(\theta,\phi) = &\int_{-l_y/2}^{l_y/2}\int_{-l_x/2}^{l_x/2} I(x',y') \\ &\times e^{j(kx'\sin\theta\cos\phi + ky'\sin\theta\sin\phi + \Phi(x',y'))}dx'dy', \end{aligned} \tag{10}$$

where l_x and l_y are the linear dimensions along the x' and y' directions, $I(x',y')$ is the source amplitude, $\Phi(x',y')$ is the phase distribution of the antenna for a rectangular-like physical aperture, and $\forall\, x' \in (\frac{-l_x}{2}, \frac{l_x}{2})$; $y' \in (\frac{-l_y}{2}, \frac{l_y}{2})$. The $SF_d(\theta,\phi)$ is then given by substituting (10) as,

$$\begin{aligned} SF_d(\theta,\phi) \approx &\int_{-l_y/2}^{l_y/2}\int_{-l_x/2}^{l_x/2} I_{fin}(x',y') \\ &\times e^{j(kx'\sin\theta\cos\phi + ky'\sin\theta\sin\phi + \Phi_{fin}(x',y'))}dx'dy'. \end{aligned} \tag{11}$$

where the required source coefficients, amplitude $I_{fin}(x',y')$ and phase $\Phi_{fin}(x',y')$ for the desired radiation pattern are reflected in (11); since SF_d was measured experimentally earlier in Section 3.2, it accounts for the effects on proximity to the car body.

The $SF_d(x,y)$ from (8) was found analytically in Stage-2, Section 3.2, using the $\gamma(x,y)$ and the experimentally measured SNR^0_{Rcv}. Since $SF_d(x,y) \rightarrow SF_d(\theta,\phi)$, the latter is known and we solve for the unknowns $I_{fin}(x',y')$ and $\Phi_{fin}(x',y')$, next.

For the inverse solution of (11), we use the Method of Moments (MoM) and the Woodward Lawson synthesis. These numerical solution techniques are used for the pattern synthesis using appropriate continuous source distributions (later presented in Section 4.3); the techniques are detailed next.

3.3.1 MoM for pattern synthesis: According to [37], Chap. 8, the MoM solution has the form of:

$$F(g) = h_e, \tag{12}$$

where h_e is the excitation function, g the response function, and $F(\cdot)$ the linear operator.

The equivalent quantities of (12) solve for the inverse solution of (11) and are:

$$\begin{aligned} &h_e(\theta,\phi) = SF_d(\theta,\phi), \quad g(x',y') = I_{fin}(x',y')e^{j\Phi_{fin}(x',y')}, \\ &F_m(g) = \int_{\frac{-l_y}{2}}^{\frac{l_y}{2}} \int_{\frac{-l_x}{2}}^{\frac{l_x}{2}} g \cdot e^{j(kx'\sin\theta_m\cos\phi_m + ky'\sin\theta_m\sin\phi_m)} dx'dy' \end{aligned} \tag{13}$$

where m is an integer. The determination of $g(x',y')$ once $h_e(\theta,\phi)$ and $F_m(\cdot)$ are known is the inverse solution to the problem (12). Since a closed-form solution is not feasible, the MoM is used and utilizes the linearity property of the $F_m(\cdot)$ for the solution of (12).

In essence, using the MoM technique, the unknown $g(x',y')$ is expressed as a linear combination of $N = N_xN_y$ in (14). N is the number of data points composing the passenger plane grid plan, Fig. 1 and $SF_d(\theta,\phi)$ is therefore sampled at N points.

$$\begin{aligned} g(x',y') &= b_1g_1(x',y') + b_2g_2(x',y') + ... + b_Ng_N(x',y') \\ &= \sum_{n=1}^{N} b_ng_n(x',y'), \end{aligned} \tag{14}$$

where, $g_n(x',y')$ is the basis function (or blending function) that is known, and b_n the unknown. Reorganizing (12) and (14) we obtain,

$$\sum_{n=1}^{N} b_nF_m(g_n(x',y')) = h_e(\theta_m,\phi_m) \quad m = 1,2....,N \tag{15}$$

where $h_e(\theta_m,\phi_m)$ is the m^{th} sample of the desired pattern $h_e(\theta,\phi) = SF_d(\theta,\phi)$ at (θ_m,ϕ_m). Since (15) contains N number of unknowns b_n, its solving is given by known samples of the pattern $h_e(\theta,\phi) = SF_d(\theta,\phi)$ taken at N points of the passenger plane grid, and the solution to this by the following Matrix,

$$\begin{aligned} &[F_m(g_n)][b_n] = [h_e(\theta_m,\phi_m)] \\ &[b_n] = [F_m(g_n)]^{-1}[h_e(\theta_m,\phi_m)] \end{aligned} \tag{16}$$

b_n is then substituted in (14) and the $I_{fin}(x',y')$ and $\Phi_{fin}(x',y')$ distributed over the physical aperture of the antenna (Fig. 4) calculated. To define g_n (16) we use the Woodward Lawson synthesis technique. Among available methods in the literature, the Schelkunoff is characterized for patterns with reduced visibility from particular directions, the Binomial and Dolph-Tschebyscheff for highly directive beams and the Fourier Transform and Woodward-Lawson for more flat (uniform) patterns; the main reason the latter was the preferred technique and is presented next.

3.3.2 Woodward Lawson for pattern synthesis: The Woodward Lawson pattern synthesis was reversely used as a source synthesis technique. The reverse method allowed for the finding of $g_n(x',y')$ and therefore for the solution of (16). Initially, the basis function (14) is rewritten [37] as:

$$g_n(x',y') = \frac{1}{l_xl_y} e^{jk\sin\theta_n(\cos\phi_nx' + \sin\phi_ny')}, \tag{17}$$

where (θ_n,ϕ_n)=(θ_m,ϕ_m) is the location of the m^{th} sample, $h_e(\theta_m,\phi_m)$, in the passenger plane. We now substitute (14) by the basis function of (17), and rearranges as,

$$g(x',y') = \sum_{n=1}^{N} \frac{b_n}{l_xl_y} e^{-jk\sin\theta_n(\cos\phi_nx' + \sin\phi_ny')}. \tag{18}$$

Using (17) and (13), the corresponding $F_m(g_n)$ is obtained and after reorganization with (16) we get,

$$\begin{aligned} F_m(g_n) =& \int_{-l_y/2}^{l_y/2} \int_{l_x/2}^{l_x/2} \left[\frac{e^{-jk\sin\theta_n(\cos\phi_nx' + \sin\phi_ny')}}{l_xl_y} \right] \\ &\times e^{j(kx'\sin\theta_m\cos\phi_m + ky'\sin\theta_m\sin\phi_m)} dx'dy', \\ F_m(g_n) =& \frac{\sin\left[\frac{kl_x}{2}(\sin\theta_m\cos\phi_m - \sin\theta_n\cos\phi_n)\right]}{\frac{kl_x}{2}(\sin\theta_m\cos\phi_m - \sin\theta_n\cos\phi_n)} \\ &\times \frac{\sin\left[\frac{kl_y}{2}(\sin\theta_m\sin\phi_m - \sin\theta_n\sin\phi_n)\right]}{\frac{kl_y}{2}(\sin\theta_m\sin\phi_m - \sin\theta_n\sin\phi_n)} \end{aligned} \tag{19}$$

By substitution, (15) becomes:

$$\begin{aligned} &\sum_{n=1}^{N} b_n \frac{\sin\left[\frac{kl_x}{2}(\sin\theta_m\cos\phi_m - \sin\theta_n\cos\phi_n)\right]}{\frac{kl_x}{2}(\sin\theta_m\cos\phi_m - \sin\theta_n\cos\phi_n)} \\ &\times \frac{\sin\left[\frac{kl_y}{2}(\sin\theta_m\sin\phi_m - \sin\theta_n\sin\phi_n)\right]}{\frac{kl_y}{2}(\sin\theta_m\sin\phi_m - \sin\theta_n\sin\phi_n)} = h_e(\theta_m,\phi_m) \end{aligned} \tag{20}$$

where $m = 1,2....,N$.

Since (20) involves the summation of b_n (N data points in the passenger plane), b_n is first solved using (16). Consequently, (18) is used to solve for the continuous source $g(x',y')$ required by the new antenna and its related synthesized source coefficients, $I_{fin}(x',y')$ and $\Phi_{fin}(x',y')$ using (13).

4 Implementation of the channel-based antenna synthesis

In this section, the implementation of the channel-based antenna synthesis for the improved in-vehicle UWB MB-OFDM communications is presented. Predicted results are performed and the simulator uses the experimentally measured channel results of Section 4.1. Following the style of Section 3, we now report the results for stages 1-3 (Fig. 2).

4.1 Stage-1: In-vehicle channel (measurements)

At this stage, the in-vehicle UWB channel was measured using the set-up configuration of Section 2 and the respective measurements, Fig. 5, subsequently presented. Microstrip printed monopole antennas (standard) from Wisair Ltd of dimensions, 38.3 mm x 28.3 mm x 0.8 mm, offering omni-directional pattern in isolation, a 2 dBi gain at the Half Power BeamWidth (HPBW), and vertical polarization were used for the access point (AP) and mobile equipment (ME) and the $h^0(t,x,y)$ and $SNR^0_{Rcv}(x,y)$ (Section 3.1) cautiously measured.

For the measurements, a PNA-X Vector Network Analyzer (VNA) form Agilent technologies was used and calibrated up to the antennas to account for possible cable and connectors inaccuracy - the antennas therefore were considered as part of the channel. Because the access point and mobile equipment antennas were connected to UWB MB-OFDM transceivers, we adopted the operation from [1] where, the access point transmitter emits a PSD of -42 dBm/MHz containing the WiMedia/ MBOA group 1 band 3.168 - 4.752 GHz (central frequency 3.4 GHz) with three sub-bands of 528 MHz and 128 point FFT each and a MB-OFDM subcarrier bandwidth calculated as 528/128 MHz. The two antennas (AP and

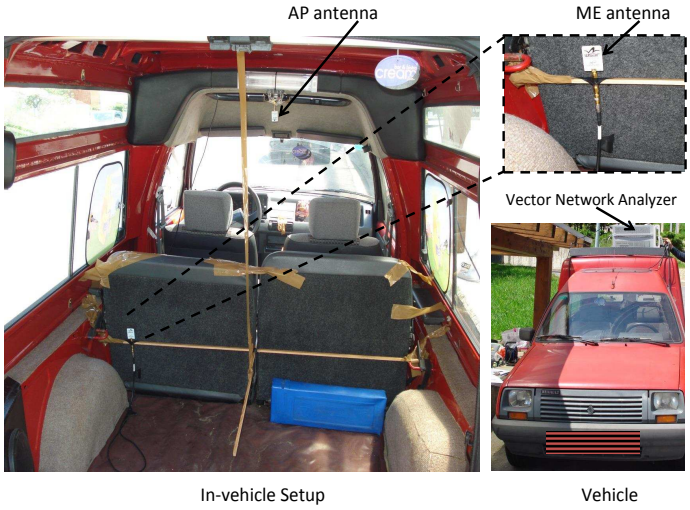

Fig. 5: Measurements of the in-car UWB channel scenario.

ME) were placed inside a Renault Extra van, Fig. 5 as reported in Section 2 and shown in Fig. 1. Whereas the access point antenna was fixed in the middle of the car ceiling, the mobile equipment was moved over the passenger plane grid for the readings.

The spacial locations (x, y) that are likely in the passenger plane are given by a sampling grid with samples defined as:

$$\begin{aligned} x[n_x] &= x[n_x - 1] + dx; \quad 1 \leq n_x \leq 20; \quad x[0] = 0, \\ y[n_y] &= y[n_y - 1] + dy; \quad 1 \leq n_y \leq 11; \quad y[0] = 0, \\ dx &= dy = 0.1m, \end{aligned} \tag{21}$$

where dx and dy are the sampling occurrence along the x and y directions, respectively. Hence, for the car dimensions of Fig. 1, the grid was sampled by $N = 220$ points. The sampling space of a radiation pattern is governed by the sampling theorem with maximum tolerable sampling separation of $\theta_m = \lambda/l$ rad [37] for its reconstruction, where l is the length of source which is 2λ (and wavelength λ corresponds to the central frequency); that leads to 0.5 radian. Since the source was at $z' = 0.8$ m distance (Fig. 4), this separation is approximated as $d_{sampling} = z' \tan(\theta_m) = 0.43$ m and samples of 0.1 m intervals have been used. This means that as the sampling distance is smaller than maximum sampling distance, the number of spatial samples was sufficient to capture all the spatial (small-scale) fading dips for the reverberating (rich multipath) environment. The mobile equipment antenna was moved over the grid (21), aided by a thin wooden-made ruler (believed not to affect the results), to measure the h^0 and SNR^0_{Rcv} at each of the distributed N points.

Only a single mobile receiver was used during the experiments (for the 220 readings) and co-existing receivers were unaccounted. This is, nevertheless, valid for retrieving a good insight of the channel impulse responses within the car. Since in co-existing receivers of multiple access protocols using time, only one time-slot is associated to each receiver, their interference is assumed meaningless [38]. Interference from other in-car devices was unaccounted and to consider these highly probabilistic interferes, a new set of measurements is desired. However, this would overhead for the use of reconfigurable antennas (to lower directivity in the direction of interferers) rather than using low cost designs planned.

4.1.1 Impulse Response, $h^0(t, x, y)$, measurement: The authors first corroborate that the occupants do not cause significant effect as in [1]. Fig. 6(a) shows the measured in-car channel IR with/without occupants when ME antenna at $x = 1$m $y = 0.6$m. As a typical IR with obstructed LOS commonly has a single cluster [39] this indicates a relatively minimal interaction of the occupants. As in [1] the ISI and BERs were found to be similar with and without occupants in this setting; the authors continue the measurements without occupants since their presence do not necessary render a different optimization result.

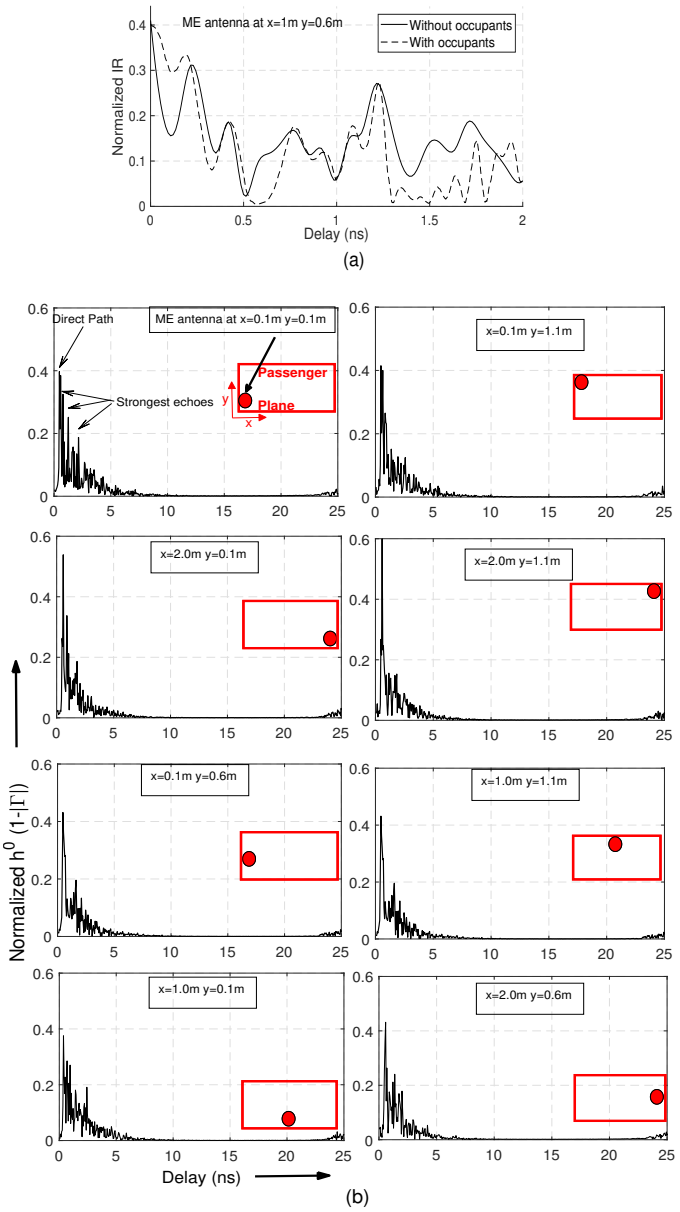

Fig. 6: Measured in-car channel IR for several mobile equipment (ME) antenna locations.

The frequency response, $H(f)$, of each N point inside the vehicle was measured in frequency domain using the VNA with range 3.168 - 4.752 GHz. The conversion to time domain was made by an Inverse Fourier Transformation (IFT); that brought the IRs (h^0) presented in Fig. 6, where the location of the mobile equipment (ME) antenna used as the probe is also illustrated. Any delay resolution due to the bandwidth (BW) was accounted for in the measurements and therefore there was no need to apply any window prior to IFT for IR side-lobe suppression. The small differ delay spreads from $\sim$0.63 ns (UWB BW) to $\sim$1 ns experimentally, implies a moderate dispersion over the signal BW; because the differential delays seen at the receiver are smaller than 1/BW and UWB resolves multipath components with differential delays of 133 ps, neglected intersymbol interference (ISI) is foreseen [1]. Although $H(f)$ was measured for N points (220 responses), only a few are shown for brevity. As

anticipated, dissimilar IR responses were observed per location and therefore reasonable to predict similar behaviors for the SNR^0_{Rcv} responses at those locations. This is corroborated subsequently.

4.1.2 Received SNR, SNR^0_{Rcv}, measurement: Following the immediately outlined channel IR measurements, the measured SNR^0_{Rcv} responses distributed over the passenger plane grid was completed and shown in Fig. 7. A steady background noise (includes

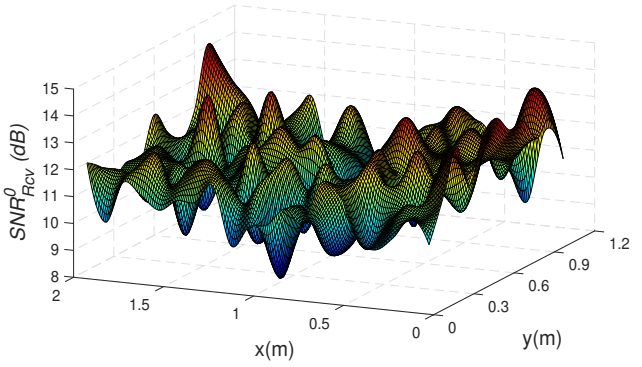

Fig. 7: Measured $SNR^0_{Rcv}(x, y)$ in-car.

noise floor) of -91 dBm was observed in-car and rapid fluctuations apparent in the passenger plane (Fig. 7). This is in line with the dissimilar IRs of Section 4.1.1, is due to the rich multipath behavior inside the car body and is corroborated by the multiple echoes of the direct path with fading (path-loss attenuation) observed in Fig. 6. The statistical properties of the measured SNR^0_{Rcv} data were: maximum 14.1 dB, minimum 8.1 dB, mean 11.1 dB, and standard deviation 0.16 dB. In addition, the highly fluctuated SNR^0_{Rcv} of Fig. 7 does not assure an equal target BER over the passenger plane grid and justifies the need of measuring the entire grid plan (N points); this is because the BER response will also fluctuate and differ from the η. Since the signal strength is dependent on the antenna efficiency, the SNR^0_{Rcv} can be improved and meet the target BER η by redefining the radiation pattern of the access point antenna, next.

4.2 Stage-2: The BER and the SF_d

In this section, the BER and the desired antenna space-factor (SF_d) performance in-car is evaluated. The adapted UWB MB-OFDM model presented in Section 3.2 is used and the UWB channel custom block redefined using a friendly graphical user interface (GUI) with setting parameters that considered the system behavior in the following communication channels, statistical AWGN, CM1 -4, and the channel measurements reported in Section 4.1. The evaluation process comprises two phases, 1) the predicted BER performance using the earlier experimentally measured in-car channel and 2) the SF_d for improved BER responses in-car.

4.2.1 The predicted BER vs. E_s/N_0 performance using the measured $h^0(t, x, y)$ and SNR^0_{Rcv}: Essentially, how the in-vehicle environment affected the channel model is shown in Fig. 8 where a deviation in the E_s/N_0 responses compared to other statistical models, CM1-4, was observed. The MB-OFDM performance was initially characterized in an AWGN channel to obtain the minimum SNR for target BER η and helped quantifying the effect of channel dispersion; the SNR was found to be ∼7.4 dB. Dissimilar SNR-BERs in each mobile equipment (ME) location encouraged measuring the multiple locations in-car and established the target SNR γ (where the BER crosses η) for 220 measured mobile equipment locations in-car; only 3 locations are shown for clarity. Results corroborate the predictions presented in Section 4.1.2, where dissimilar BER performances were anticipated in the passenger grid plan (N points). This justifies the use of the 220 readings (a high number means accuracy) and the practical on-site measurements overcome unrealistic statistical channels in this application - unrealistic because these canonical form channels do not fully describe the in-car application presented in this manuscript. The slightly improved performance on CM4 over the CM1 (LOS) was due to the car body acting as a reverberation channel which favored from the collection of multipaths.

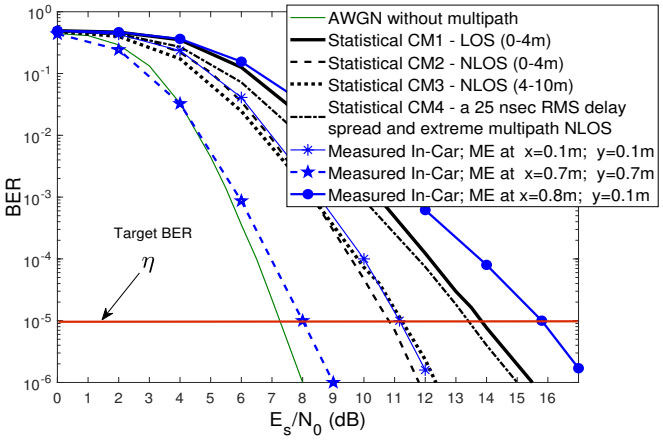

Fig. 8: BER vs. E_s/N_0 using statistical and measured channels with different IRs.

4.2.2 The $SF_d(x, y)$ that attains the target BER performance in the passenger plan (N points): For the assessment, $\gamma(x, y)$ is calculated using (4) and $\gamma = E_s/N_0 \times (f_s/B)$, where f_s is the channel data rate and B the bandwidth. The result is plotted in Fig. 9(a) and shows a $\gamma(x, y)$ as dictated by the $\eta = 10^{-5}$ (Fig. 8). A histogram, presented in Fig. 9(b), shows the highly varied γ responses over the passenger plane grid, corroborates the need of measuring N points, and prevails over the predominantly use of statistical channel models for their lack of accuracy (scarce number of registered data points [17–23]) in this application.

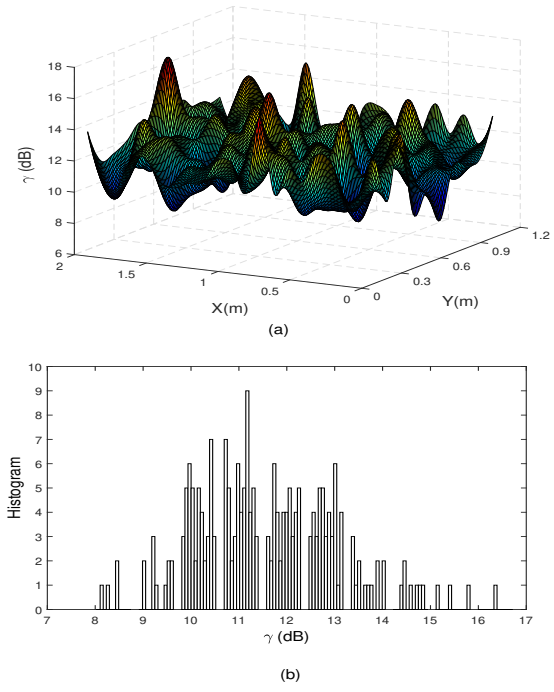

Fig. 9: (a) The calculated $\gamma(x, y)$ in-car, and (b) the histogram of the γ.

Following the calculated $\gamma(x, y)$, the $SF_d(x, y)$ was found. For the calculation, (8), evolving the SNR^0_{Rcv} (Fig. 7) and the γ (Fig. 9a), was used. The result is plotted in Fig. 10 and used to optimize the physical aperture of the prospective antenna and its associated continuous source distribution, next.

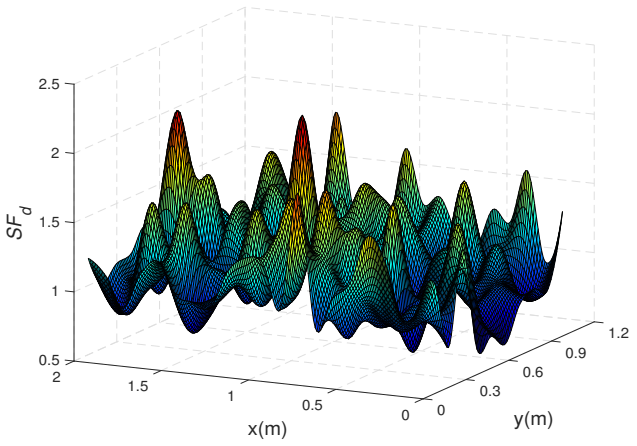

Fig. 10: The calculated desired antenna space-factor $SF_d(x, y)$ in-car.

4.3 *Stage-3: Radiation pattern-and-source synthesis*

The physical aperture and associated continuous source distribution of the prospective antenna is now determined. Particularly, the Woodward-Lawson pattern synthesis technique introduced in Section 3.3.2 and the SF_d response presented in Fig. 10, is used to determine the required continuous source, $I_{fin}(x', y')$ and $\Phi_{fin}(x', y')$. The SF_d was obtained using 220 N points since a higher number of samples in (20) yields to a highly complex inverse operation to matrix (16). Hence, we limited the number of samples to N_s, $\rightarrow N_s \leq N$. Due to the limitations of using N_s (rather than N), the BER adjusts to BER^{fin} and hence to SF_{fin}. Since N_s defines the physical aperture of the antenna, Fig. 4, whose dimensions $l_x = l_y = \lceil\sqrt{N_s}\rceil\lambda$, [37], the lower the N_s, the smaller the aperture (preferred). But, as N_s impacts on the BER performance (later corroborated in this Section), we established herein a prospective antenna design whose N_s is the optimization parameter to minimize the blind spots (1) in-car.

To find the continuous source (18) required by the antenna we rearranged the initial goal (2) such that the optimization problem becomes:

$$\begin{aligned} &\underset{N_s}{\text{Minimize}} \quad \%\text{Blind Area}\,(1) \\ &\text{subject to} \quad N_s \leq N, \end{aligned} \tag{22}$$

To determine the appropriate N_s value, we close looked at the individual $N = 220$ samples of the SNR^0_{Rcv} (Fig. 7) and selected those samples with deprived SNR; the selected samples correspond to those deeply faded responses in the passenger grid plan. To improve the received signals in-car and the BER consequently, we computed the minimum blind-area solution probable and the continuous source coefficients for that solution, next.

4.3.1 The optimization of the blind-areas in-car: We used (22) and the Woodward-Lawson synthesis of Section 3.3.2 for the purpose and plot aided by Matlab the percentage blind-area in regards to N_s in Fig. 11. The response is non-monotonic with N_s settled to the adopted scheme and not to a synthesized antenna size. By observation, the overall blind-area is N_s dependent and severely varies upon N_s. Furthermore, values of $N_s > 17$ have no real solution since the inverse matrix calculation of the invertible square matrix (16) is singular (not feasible) to working precision. Therefore

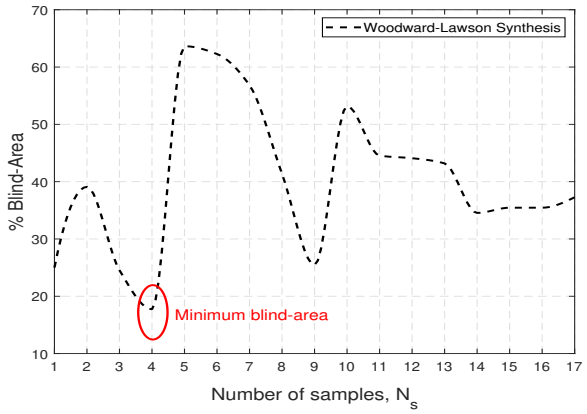

Fig. 11: The minimum blind-area in-car used for optimization.

N_s is limited to $1 \leq N_s \leq 17$ and the optimized solution to (22) found to be $N_s = 4$ (the lowest blind-area in Fig. 11). This is in fact the 4 lowest SNRs in the passenger grid plan and will be demonstrated, later in Section 5, to be an optimal value for the improved BER performances in-car.

4.3.2 The required continuous source coefficients: We used the immediately reported $N_s = 4$, which in fact corresponds to 4 optimal samples of the SF_d (Fig. 10). Since the continuous source coefficients (amplitude and phases) can be found from the SF_d (by finding $[b_n]$), Section 3.3.2, hence, we use the inverse pattern synthesis technique to retrieve every $I_{fin}(x', y')$ and $\Phi_{fin}(x', y')$ composing the prospective antenna's physical aperture. The result is depicted in Fig. 12, and leads to an antenna (Fig. 4) of dimensions $l_x = l_y = \lceil\sqrt{N_s}\rceil\lambda = 2\lambda$. Using the antenna's physical aperture as

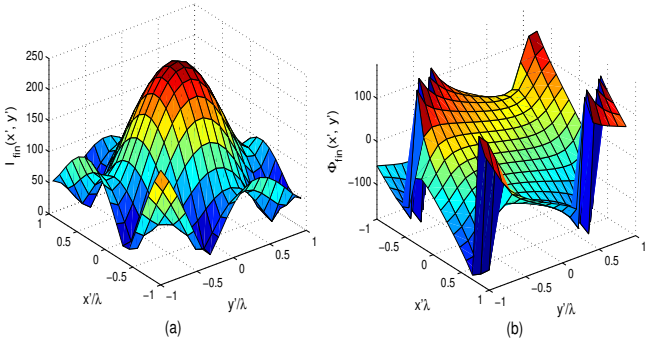

Fig. 12: Required continuous source coefficients (a) $I_{fin}(x', y')$ (b) $\Phi_{fin}(x', y')$ showing the prospective antenna's physical aperture in regards to wavelength, λ.

a contribution of the continuous source coefficients immediately outlined (shown in Fig. 12), the $SF_{fin}(x, y)$ of the prospective antenna is calculated and the result depicted in Fig. 13. Primarily given by the computational limitations of $N_s \leq N$ and the inherent antenna's aperture dimensions, the SF_{fin} differed from the SF_d, but did not present inhibition for improving the UWB MB-OFDM communications in-car. This is corroborated in the results section, subsequently.

5 Results

The improved in-vehicle UWB MB-OFDM communications is evidenced from the improved responses (BER and blind-area) obtained when using the prospective antenna compared to the standard and is detailed next.

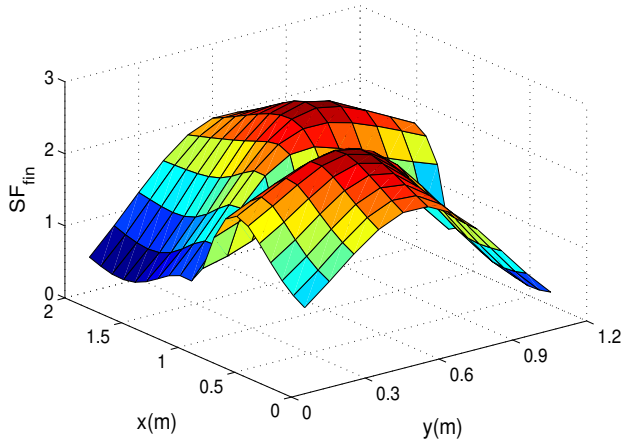

Fig. 13: The calculated $SF_{fin}(x, y)$ in-car using the prospective antenna as access point.

5.1 The improved BER

Using the adapted Simulink model presented in Section 3, the BER performance in-car is predicted when using the standard antenna and the prospective antenna for the access point. Comparison results show the $BER^{0}(x, y)$ vs. the $BER^{fin}(x, y)$, in Fig. 14(a) and (b) respectively, distributed over the passenger grid plan in a color map surface plot form. By observation, the BER performance in-

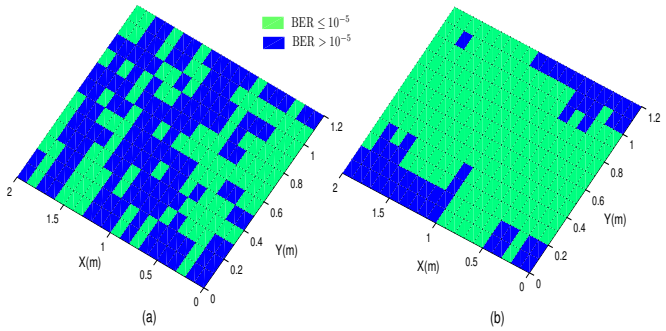

Fig. 14: The predicted BER in-car (a) BER^{0} using the standard antenna (b) BER^{fin} using the prospective antenna

car is outperformed for the case where the prospective antenna is used since a far inferior number of blind-areas ($BER > 10^{-5}$) are apparent. The blind areas still present in Fig. 14(b) depended on the selection of the N_s samples that were used for optimization. This value was limited upon the antenna realization (realistic size) to 4 (Section 4.3) and led to few error rates in certain points of the grid plan. Yet, a largely improved error rate is seen as a whole. The accomplished $BER^{fin}(x, y)$ is therefore principally achieved as a result of the well-defined c ontinuous source coefficients, $I_{fin}(x', y')$ and $\Phi_{fin}(x', y')$) of Fig. 12.

5.2 The improved blind-area

Using the results of Fig. 14, the percentage blind-area was computed for comparison between the responses of the prospective antenna vs. those of the standard when used as access point. The comparison is provided in Table 1 and the result achieved by the prospective antenna reduced the %Blind-Area (1) in 37.73% compared to that of the standard antenna. This translates into high-efficient (capacity and data rate) UWB-OFDM communications in-car.

Table 1 Performance comparison when using the prospective antenna vs. the standard antenna for the access point.

	% Blind Area
Standard Antenna	55.45%
prospective Antenna	17.72%

5.3 Feasible antenna solution

The prospective antenna gained from this research contribution is given by continuous source coefficients (amplitudes and phases) composing the antenna's physical aperture. The fabrication of this feasible antenna is suggested as future research. Although the rectangular-like planar aperture of the antenna ($l_x = l_y = 2\lambda$) was found tolerable for the in-car application, to exactly reflect the $I_{fin}(x', y')$ and $\Phi_{fin}(x', y')$ on a continuous antenna aperture (i.e: a patch) needs to be addressed, but seems to be a better solution than an array-made antenna since the feeding network of the array would be large and lossy. The antenna-array becomes large since multiple source coefficients would be required to form the array elements. A discretization of the continuous source (e.g., discrete source) can be used to estimate the radiation pattern of the antenna close to the SF_d [37]. The accuracy of this radiation pattern depends on the sampling occurrence, the permissible difference between the SF_d and the approximate pattern, and the BER_{fin}. The sampling can be met using the Root-Matching and perturbation techniques [40]; all have their own limitations over accuracy. Prototypes based on dielectric-made domes for shaping the antenna's radiation pattern [41] are suggested for investigation using the hereby proposed channel-based antenna synthesis; that would bring antennas with spatially selective gains, ideal for the antenna solution.

6 Conclusion

A channel-based antenna synthesis for improved in-vehicle UWB MB-OFDM communications has been proposed and presented. The synthesis allows for optimizing an antenna design for the scenario. The radiation pattern (an optimized SF) of the antenna (given by continuous source coefficients and a rectangular-like planar aperture) was modeled to provide improved in-vehicle UWB communications. This was achieved by an antenna whose SF provided (uniform) SNR-BER response in the passenger plane in-car and attributed to lowering the blind spots in the plane. Although this synthesis can be applicable to other vehicles, the extrapolation of the contemporary SF is limited to cars of similar dimensions since the IRs of the channel would vary. Any variation in the channel might not significantly influence on the primary antenna selection, but if a fully customized antenna is desired a new set of measurements should be performed. To corroborate the improved BER performance in-car, the results obtained using the prospective antenna were compared to those of a standard antenna. A new set of in-car channel measurements was performed, using the standard antenna, to overcome the unrealistic behavior of existing channel models in this scenario. The BERs were predicted using this genuine channel and provided the basis for estimating the SF of the access point antenna. The use of the prospective antenna showed an alleviated blind-area performance compared to that using the standard antenna and supports the optimized design (SF + continuous source coefficients + rectangular-like planar aperture) as a candidate for the access point in high-efficient UWB-OFDM communications in-car.

7 References

1 I. J. Garcia Zuazola, J. M. H. Elmirghani, and J. C. Batchelor, "High-speed ultra-wide band in-car wireless channel measurements," *IET Communications*, vol. 3, no. 7, pp. 1115 – 1123, July 2009.

2 I. J. G. Zuazola, L. Azpilicueta, A. Sharma, H. Landaluce, F. Falcone, I. Angulo, A. Perallos, W. G. Whittow, J. M. H. Elmirghani, and J. C. Batchelor, "Band-pass filter-like antenna validation in an ultra-wideband in-car wireless channel," *IET Communications*, vol. 9, no. 4, pp. 532 – 540, March 2015.

3 "First report and order, revision of part 15 of the commissions rules regarding ultra-wideband transmission systems," FDD, Tech. Rep. ET Docket 98-153, Feb.

2002.
4 S. Roy, J. Foerster, V. Somayazulu, and D. Leeper, "Ultrawideband radio design: the promise of high-speed, short-range wireless connectivity," *Proc. IEEE*, vol. 92, no. 2, pp. 295–311, Feb. 2004.
5 A. Batra and et al., "Multiband OFDM physical layer specification," WiMedia Alliance, Release 1.1, July 2005.
6 V. S. Somayazulu, J. R. Foerster, and S. Roy, "Design challenges for very high data rate UWB systems," in *Asilomar on Systems, Signals, and Computation*, Nov 2002, pp. 717 – 721.
7 IEEE 802.15 WPAN High Rate Alternative PHY Task Group 3a (TG3a). [Online]. Available: http://www.ieee802.org/15/pub/TG3a.html
8 A. Batra and et .al., "TI physical layer proposal for IEEE 802.15 task group 3a," IEEE P802.15-03/142r2-TG3a, March 2003.
9 ——, "Multi-band OFDM physical layer proposal," IEEE P802.15-03/268r0-TG3a, July 2003.
10 *ECMA-368*, Std., December 2008. [Online]. Available: http://www.ecma-international.org/publications/standards/Ecma-368.htm
11 S. H. Kratzet, "MB-OFDM and DS-UWB ultra-wideband design using SystemView by Elanixw," Eagleware-Elanix App Note AN-24B, March 2005.
12 G. Khuandaga, A. Iqbal, and K. S. Kwak, " Analysis of Modulation Schemes in Intra Vehicle Communications (IVC) Channel," in *13th International Conference on Advanced Communication Technology (ICACT)*, Feb. 2011, pp. 725–729.
13 X. Yin, J. Liu, Y. Su, X. Xiong, and G. Xiong, "A low-complexity synchronizer for OFDM-UWB-based vehicular communications," *IEEE Access*, vol. 5, pp. 7272–7284, 2017.
14 A. Batra, J. Balakrishnan, G. R. Aiello, J. R. Foerster, and A. Dabak, "Design of a Multiband OFDM System for Realistic UWB Channel Environments," *IEEE Transaction on Microwave theory and Techniqques*, vol. 52, no. 9, pp. 2123–2138, Sept. 2004.
15 J. Foerster, "Channel modeling sub-committee report final," *IEEE, P802.15-02/368r5-SG3a*, 2002.
16 A. Saleh and R. Valenzuela, "A statistical model for indoor multipath propagation," *IEEE Journal on selected areas in communication*, vol. 5, no. 2, pp. 128–137, Feb. 1987.
17 P. C. Richardson, W. Xiang, and W. Stark, "Modeling of Ultra-Wideband Channels Within Vehicles," *IEEE Journal on selected areas in communication*, vol. 24, no. 4, pp. 906–912, april 2006.
18 Y. Katayama, K. Terasaka, K. Higashikaturagi, I. Matunami, and A. Kajiwara, "Ultra-Wideband Impulse-Radio Propagation for In-Vehicle Wireless Link," in *64th IEEE Vehicular Technology Conference, VTC Fall*, Montreal, Quebec, Canada, 25-28 September 2006.
19 W. Niu, J. Li, and T. Talty, "Intra-vehicle UWB channels in moving and staionary scenarios," in *IEEE MILCOM*, Oct. 2009, pp. 1–6.
20 J. Mar, Y.-C. Yeh, and C.-C. Kuo, "Novel UWB In-Vehicle Channel Measurement Approach Based on Chirp Pulse Sounding Signal," in *International Symposium on Intelligent Signal Processing and Communication Systems (ISPACS 2009)*, Dec. 2009.
21 Y. Jin, D. Kwak, and K. S. Kwak, "Performance Analysis of Intra-vehicle Ultra-Wide Band Propagation in Multi-user Environments," in *IEEE 1st International Workshop on Vehicular Communications, Sensing, and Computing (VCSC)*, June 2012.
22 D. W. Matolak and A. Chandrasekaran, "5 ghz intra-vehicle channel characterization," in *IEEE Vehicular Technology Conference (VTC Fall)*, 2012, pp. 1–5.
23 C. U. Bas and S. C. Ergen, "Ultra-wideband Channel Model for Intra-vehicular Wireless Sensor Networks Beneath the Chassis: From Statistical Model to Simulations," *IEEE Transaction on Vehicular Technology*, vol. 62, no. 1, pp. 14–25, Jan. 2013.
24 A. Chandra, A. Prokeš, T. Mikulášek, J. Blumenstein, P. Kukolev, T. Zemen, and C. F. Mecklenbräuker, "Frequency-domain in-vehicle UWB channel modeling," *IEEE Transactions on Vehicular Technology*, vol. 65, no. 6, pp. 3929–3940, June 2016.
25 T. Kayser, J. V. Hagen, and W. Wiesbeck, " of antenna locations for wireless incar communication," in *URSI Int. Symp. Electromagnetic Theory*, Pisa, Italy, May 2004.
26 M. A. Peyrot-Solis, G. Galvan-Tejada, and H. Jardon-Aguilar, "State of the art in ultra-wideband antennas," in *2nd International Conference on Electrical and Electronics Engineering (ICEEE) and XI Conference on Electrical Engineering (CIE)*, Mexico City, Mexico, September 7-9 2005, pp. 101–105.
27 Z. shunshi, L. Xianling, and Y. Xiaorong, "UWB planar antenna technology," *Chinese Journal of Radio Science*, vol. 22, no. 2, pp. 308–315, April 2007.
28 W.-S. Lee, D.-Z. Kim, K.-J. Kim, and J.-W. Yu, "Wideband Planar Monopole Antennas With Dual Band-Notched Characteristics," *IEEE Transactions on Microwave Theory and Techniques*, vol. 54, no. 6, pp. 2800–2806, June 2006.
29 C. Yong, LuiWen-jun, C. Chong-hu, and C. Wei, "A compact frequency notched ultra-wideband antenna for multiple application," *Journal of Microwaves*, vol. 23, no. 1, pp. 20–24, Feb. 2007.
30 H. Deng, X. He, S. Liu, and Y. Xie, "A Novel Ultra Wideband Planar Antenna," in *Global Symposium on Millimeter Waves, GSMM*, 2008, pp. 288 – 290.
31 S. Adnan, R. A. Abd-Alhameed, S. Jones, H. I. Hraga, M. S. Bin-Melha, and E. A. Elkhazmi, "A modified printed monopole antenna for ULTRA-WIDEBAND applications," in *Proceedings of the Fourth European Conference on Antennas and Propagation (EuCAP)*, April 2010.
32 A. A. Kishk, X. H. Wu, and K. S. Ryu, "UWB Antenna for Wireless Communication and Detection Applications," in *IEEE International Conference on Ultra-Wideband (ICUWB)*, Sept. 2012, pp. 72–76.
33 I. J. Garcia Zuazola, J. C. Batchelor, J. M. H. Elmirghani, and N. J. Gomes, "UWB PIFA Antenna for simplified transceivers," *IET Electronics Letters*, vol. 46, no. 2, pp. 116–118, Jan. 2010.
34 H. Deng, J. Li, L. Yang, and T. Talty, "Intra-Vehicle UWB MIMO Channel Capacity," in *IEEE Wireless Communications and Networking Conference Workshops*, paris, April 2012, pp. 393–397.
35 A. Goldsmith, *Wireless Communications*. Cambridge University Press, NY, 2005.
36 M. Clark, M. Mulligan, and D. Jackson, "Fixed-Point Modeling in an Ultra Wideband Wireless Communication System," Matlab digest, May 2004.
37 C. A. Balanis, *Antenna Theory Analysis and Design*, 2nd ed. Wiley, 1997.
38 Y. Li, Y. Wang, and J. Lu, "Performance Analysis of Multi-User UWB Wireless Communication Systems," in *International Conference on Wireless VITAE*, Aalborg, Denmark, May 2009, pp. 152–155.
39 U. G. Schuster and H. Bolcskei, "Ultrawideband channel modeling on the basis of information-theoretic criteria," *IEEE Transactions on Wireless Communications*, vol. 6, no. 7, pp. 2464–2475, July 2007.
40 R. S. Elliott, "On discretizing continuous aperture distributions," *IEEE Transaction on Antennas and propagation*, vol. 25, no. 5, pp. 617–621, Sept. 1977.
41 N. T. Nguyen, A. V. Boriskin, A. Rolland, L. L. Coq, and R. Sauleau, "Shaped Lens-Like Dome for UWB Antennas With a Gaussian-Like Radiation Pattern," *IEEE Transaction on antennas and propagation*, vol. 61, no. 4, pp. 1658–1664, April 2013.